J Solid State Electrochem (2007) 11:1127–1131
DOI 10.1007/s10008-006-0249-1

ORIGINAL PAPER

Synthesis, characterization and lithium-intercalation properties of rod-like $CaMoO_4$ nanocrystals

Yongguang Liang · Xiaoyan Han · Zonghui Yi · Wenchao Tang · Liqun Zhou · Jutang Sun · Shuijin Yang · Yunhong Zhou

Received: 14 August 2006 / Revised: 6 November 2006 / Accepted: 17 November 2006 / Published online: 3 January 2007

Abstract Rod-like $CaMoO_4$ nanocrystals were synthesized via a template-based rheological phase reaction route as a novel method. The physical characterization was carried out by thermogravimetric/differential thermal analysis (TG/DTA), X-ray diffraction (XRD), scanning electron microscopy (SEM), transmission electron microscopy (TEM), and elected-area electron diffraction (SAED). A structure-directed role of hexamethylene tetramine (HMTA) was observed during the formation of $CaMoO_4$ nanocrystals. The electrochemical performance of $CaMoO_4$ as anode for lithium ion batteries has also been investigated by galvanostatic cycling and AC impedance spectroscopy. $CaMoO_4$/Li cell can deliver superior capacity than theoretical value in the initial cycle, and the much improved capacity was attributed to the contribution of oxygen besides the reduction of molybdenum during lithium insertion. Furthermore, a charge capacity of 276 and 438 mAh/g was retained after 50 cycles in the range of 0.01–2.50 V vs Li at a current density of 100 and 200 mA/g, respectively. The particle size and morphological properties were found to play an important role in fast lithium insertion/extraction performance and cycling stability at high rate.

Keywords $CaMoO_4$ · Nanomaterials · Electron microscopy · Anode materials · Lithium ion batteries

Y. Liang (✉) · X. Han · Z. Yi · W. Tang · L. Zhou · J. Sun · S. Yang · Y. Zhou
Department of Chemistry, Wuhan University, Wuhan 430072, People's Republic of China
e-mail: ygliang@mail.whu.edu.cn

Introduction

Electrochemical capacitors with high power density are attractive energy storage devices for high power applications like electric vehicles and pulsed lasers [1–3] and are called "supercapacitors," generally. Supercapacitors using Li^+ insertion reaction into electrode materials, which use another faradaic process, are expected to show both high-energy capability and power density. Carbonaceous materials [4–6], tin-based oxides and alloys [7–10], transition metal oxides [11–13] and composite oxides [14–16] are known as a host for lithium insertion. However, the diffusion of Li^+ in the solid phase is rather slow, and the electronic conductivity of intercalation hosts is usually too low to sustain large currents. In comparison with the many studies on the improvement of capacity density, electrode properties of these materials at large currents have been less studied.

It is known that the rate of ionic diffusion through the electrode particle is slow relative to the effective current density (the rate of charge transfer at the surface) [17]. To a large particle, a radial lithium concentration gradient within the electrode will appear inevitably due to the polarization, and hence, an inefficient charge/discharge. Smaller grain size can effectively lessen the polarization by reducing lithium ion and electron diffusion distances to favor Li^+ ions mobility within the electrode. Therefore, nanoparticulate electrodes are often used to achieve significant enhanced capacity and rate performance at high current rate [18, 19]. Currently, it seems that transition metal oxides and composite oxides are the systems of potential choice for high rate electrodes [18], which offer promises to enlarge the application of lithium secondary batteries in high-power devices.

In this paper, we introduced a novel method to the preparation of rod-like $CaMoO_4$ nanocrystals through a template-based rheological phase reaction route using hexamethylene tetramine (HMTA) as a structure-directed agent. The electrochemical performance of $CaMoO_4$ has also been investigated, and the superior capacity retention and cycling stability were found to have a correlation with their nature of nanostructure.

Materials and methods

The precursor was synthesized by a HMTA-assisted rheological phase reaction [20]. All reagents were analytical grade and used without further purification. $(NH_4)_6Mo_7O_{24}{\cdot}4H_2O$, 1.77 g, and 2.82 g HMTA were fully mixed by continuous grinding and dropping proper absolute ethanol in intervals to get a clear gel. After added stoichiometric $Ca(Ac)_2{\cdot}2H_2O$, the mixture was sealed in a closed Teflon-lined stainless autoclave for 4 h at 80 °C and dried under vacuum. The precursor was finally obtained and treated at 500 °C in air for 4 h to give a $CaMoO_4$ product.

Powder X-ray diffraction was carried out on a high-resolution Bruker AXS D8 diffractometer using monochromatic Cu $K_{\alpha 1}$ radiation (1.54056 Å), selected by an incident beam Ge Johannson monochromator, equipped with a receiving slit of 0.1 mm and a Sol-X detector in the 2θ range from 10 to 120 °. Data were collected using a constant step scan of 0.01 ° per step and were normalized to a constant acquisition time of 5 s.

The thermal stability of the precursor was examined by means of thermogravimetric (TG) and differential thermal analysis (DTA) curves with a Netzsch STA 449 thermal analysis system at a heating rate of 10 °C/min from 25 to 750 °C in a flow of air. The morphological features were observed by a scanning electron microscope (Hitachi SEM X-650). Crystalline phase was tested with transmission electron microscopy (TEM) and elected-area electron diffraction (SAED) on a transmission electron microscope (JEOL JEM2010FEF). AC impedance measurements of electrodes were performed on a CHI760C by applying an AC voltage of 5 mV amplitude in the frequency range 100 KHz to 1 mHz.

The charge/discharge tests were carried out using the coin-type cell (size: 2016), which consists of a working electrode and a lithium foil counter electrode separated by Celgard 2400 microporous membrane. Electrodes were prepared by mixing $CaMoO_4$ powders with 10 wt% acetylene black and 5 wt% polytetrafluoroethylene (PTFE). A 1 mol/l solution of $LiClO_4$ dissolved in ethylene carbonate (EC)/diethyl carbonate (DEC) (1:1, volume) was used as the electrolyte. $CaMoO_4$/Li cells were tested between 2.5 and 0.01 V vs Li at a different current density.

Results and discussion

Typical TG and DTA curves of the precursor are shown in Fig. 1. The trace shows two major events. The mass loss of about 6.5% occurs before 200 °C, corresponding to the loss of absorbed water and ammonia. There is a complicated pyrolysis stage in the region of 200–422 °C. The endothermic peaks at about 252 and 348 °C on the DTA curve give two thermal behaviors. One is the decomposition reactions of acetic salts and ammonium salts. The other is the simultaneous reactions of gaseous resultants with oxygen. Thus, the endothermic behaviors are the combination of decomposition reaction and reoxidation process. Subsequent unobvious peak at 423 °C is attributed to the final process of calcium and molybdenum oxides to form a $CaMoO_4$ phase.

Figure 2 illustrates the refined powder XRD profiles of the product. The WinPLOTR program [21] was used for peak position calculation and the automatic indexation was conducted with the DICVOL04 program [22] against the first 21 experimental diffraction peaks. A tetragonal solution was found with unit-cell parameters, a=5.21365 (3)Å and c=11.3868(7)Å with the following figures of merit: M_{20}=214.1, F_{20}=236.3. Model-based refinements of whole profile and structural parameters yield to the following reliability factors: R_{obs}=5.58%; R_p=6.25; R_{wp}= 6.93 with all the isotropic atomic displacement parameters defined. The best solution is suggested with unit-cell parameters, I 1/a space group, a=5.22865(3)Å and c= 11.4368(5), V=312.360 (11) $Å^3$, Z=2.

The particle sizes and morphological features of $CaMoO_4$ samples were characterized by scanning electron microscopy (SEM) and TEM observations as shown in Fig. 3. We can see two characteristic morphologies of the rods in Fig. 3a. Most of the rods are dispersive with particle size about 70 nm in diameter. However, bar-like particles

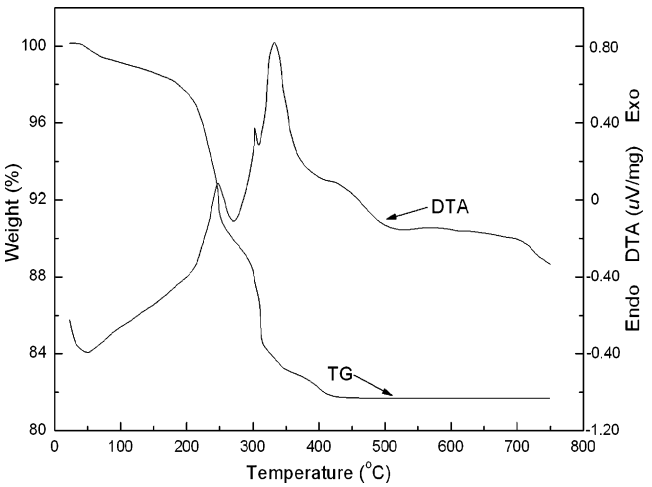

Fig. 1 TG and DTA curves of the precursor

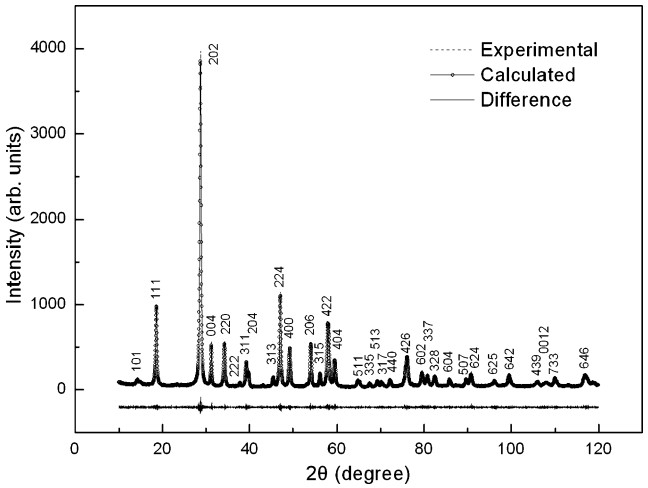

Fig. 2 Whole-powder-diffraction-pattern-refined profiles of the resulted $CaMoO_4$ sample

can also be seen in different regions with breadth ranging from 160 to 220 nm. A closer inspection of the shape reveal that these bars are composed of three or more single rods arranged closely along the vertical direction to rod growth, which indicates two possible different processes of the growth of crystals. Figure 3b shows the typical image of one-dimensional nanorods, and a twinning crystalline nature of the $CaMoO_4$ nanorods was confirmed by the inset corresponding characteristic SAED pattern. Further experiments were also conducted to understand the reaction process of the present experiment. Figure 3c and d provide the typical images of the precursors with different reaction times of 1 and 4 h. A self-assembled process directed by HMTA becomes complete with the increasing reaction time, and the morphology of the precursor changes from conglomeration (Fig. 3c) to a visible one-dimensional orient (Fig. 3d). On the basis of the aforementioned experimental results and the image of bulk sample without an additive of HMTA (see Fig. 5a), a possible reaction process might be described as following: isolative Ca^{2+} and MoO_4^{2-} ions diffuse very slowly in the mixed inorganic and organic phase. Mo^{6+} ions assembled by the direction role of HMTA ligand yield an oriental array. The temperature increases the slow diffusion rate of ions in some extent, and Ca^{2+} ions react with direction-selected $Mo(L)_x^{n-}$ to give oriented $CaMoO_4$ with the increase of reaction time. Rod-like precursor was then used as a template in the later thermal treatment to yield $CaMoO_4$ nanorods. This new

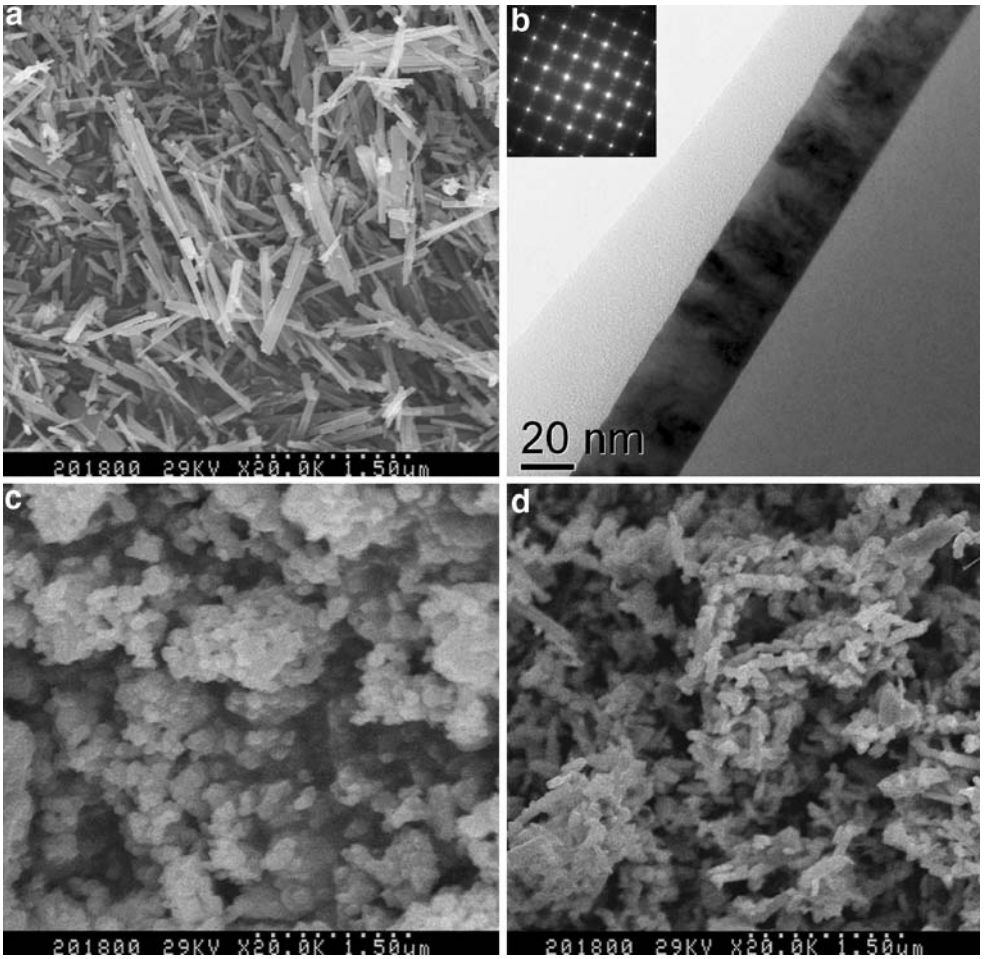

Fig. 3 Microstructures of $CaMoO_4$ nanocrystals and the precursors: **a** SEM image of $CaMoO_4$ nanorods; **b** TEM and SAED images of rod-like $CaMoO_4$ nanocrystals; **c** SEM image of the precursor for 1 h; **d** SEM image of the precursor for 4 h

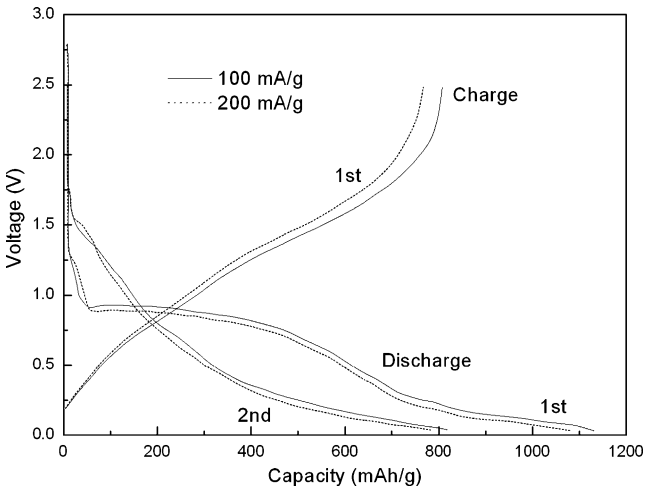

Fig. 4 Discharge and charge curves of $CaMoO_4$/Li test cell at different current rates

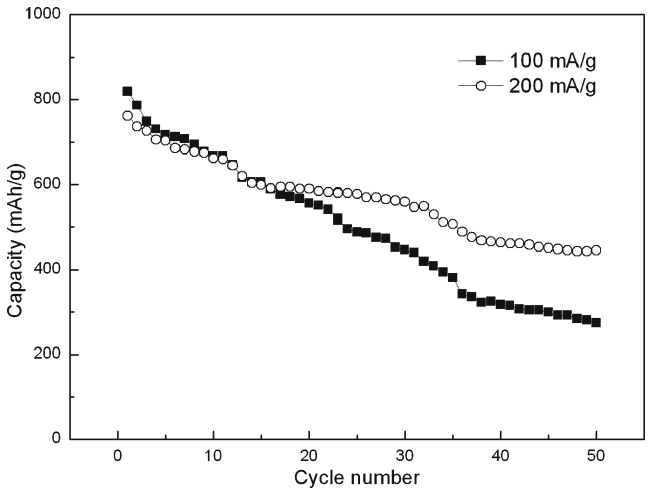

Fig. 6 Cycling performance of $CaMoO_4$/Li test cell at different current rates

adaptable structure prompted us to construct different morphologies in which sizes and chemical environments could be varied [23].

The discharge–charge curves of $CaMoO_4$/Li test cell recorded with different current rates are presented in Fig. 4. During the initial Li-insertion process, an irreversible structural transition into amorphous phase took place within $CaMoO_4$ electrode [24]. The potential slope at about 1.25 V indicates the formation of solid electrolyte interface (SEI) and the irreversible reaction of lithium with oxygen atoms in the active material. Subsequent plateau at 0.90 V reveals an amorphization. The discharge capacity of $CaMoO_4$ during the first discharge comes to 1,134 and 1,082 mAh/g in the voltage range of 0.01–2.50 V at a current density of 100 and 200 mA/g, respectively. However, the theoretical capacity value for the first discharge involving crystal structure destruction and reduction of the Mo^{6+} to Mo^0 in $CaMoO_4$ is 804 mA h/g (6 mol of Li). The Ca^{2+} ion in $CaMoO_4$ is not expected to be reduced to Ca metal under room-temperature electrochemical conditions, and this can be understood by a consideration of free energies of formation. The value of CaO (−144.37 kcal/mol) is more negative than that of Li_2O (−134.13 kcal/mol) [25]. Figure 4 also shows reoxidation of Mo to +4 at 2.0 V during the lithium removal process. The charge capacity of $CaMoO_4$ during the first cycle arrives at 812 and 763 mAh/g at a current density of 100 and 200 mA/g, respectively. The valence change in Mo is not enough to explain the much improved capacity of $CaMoO_4$ and the state of Ca, which is more reduced than Ca^{2+}, is difficult to imagine. Thus, it is conceivable that there is the contribution of oxygen besides the reduction/oxidation of Mo during lithium insertion/extraction. Obviously, the electrode characteristics of $CaMoO_4$ nanocrystals is correlated with their nanostructured nature, which is much affected by particle size and morphological properties.

To provide more information of the electrochemical properties affected by particle sizes, AC impedance was performed on two samples with different particle sizes. Figure 5a gives a SEM image of another $CaMoO_4$ sample prepared without an additive of HMTA. As we can see, the particle size and morphological features are obviously different from $CaMoO_4$ nanocrystals in Fig. 3a. The particles are agglomerated with irregular shape ranging in

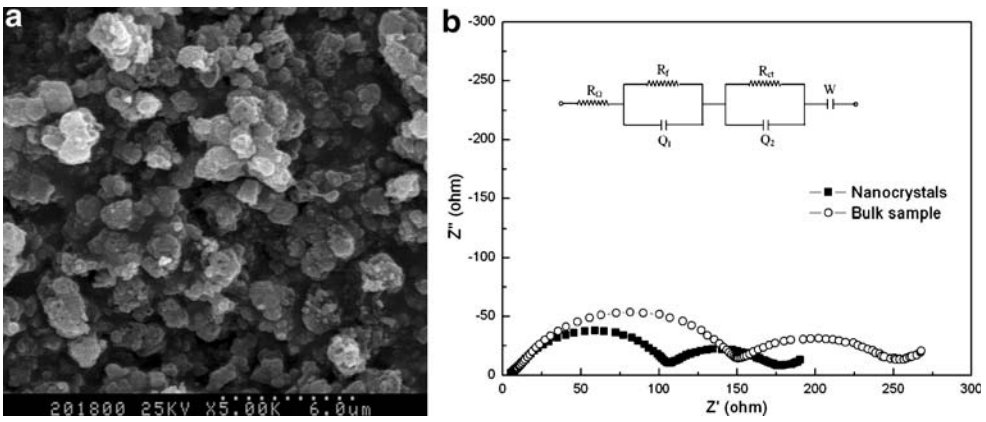

Fig. 5 **a** SEM image of CaMoO4 sample without an additive of HMTA; **b** Ac impedance spectra of different $CaMoO_4$/Li test cells discharged to 0.01 V in the initial cycle

size from 1.8 to 6 μm. Figure 5b shows typical impedance spectra of two samples obtained at 0.01 V potential in the first discharge at a current density of 100 mA/g. Two typical semicircles and one slope were observed in both spectra. An intercept at the Z_{real} axis in high frequency corresponds to the ohmic resistance (R_Ω), which represents the total resistance of the electrolyte, separator, and electrical contacts. The depressed semicircle in the high frequency range was related to the Li ion migration resistance (R_f) through the SEI film formed on the electrode or another coating layer. The second semicircle in the middle frequency range indicates the charge transfer resistance (R_{ct}). The slope in the lower frequency shows the Warburg impedance, which is associated with lithium-ion diffusion in the $CaMoO_4$ particles. Simplified equivalent circuits models were constructed to analyze the impedance spectra in the inset model of Fig. 5b. The parameters of the equivalent circuit (R_Ω, R_f, and R_{ct}) for nanosized $CaMoO_4$ and bulk one were suggested by computer simulations (Zview®): 5.22, 54.7, 35.9; 6.08, 72.2, 57.6. The lower R_Ω for nanocrystal sample indicates a lower inner resistance of the cell. The values of R_f and R_{ct} ascend with the increase of the particle size, partly explaining the higher initial capacity of nanosized $CaMoO_4$ electrode in Fig. 4.

Figure 6 shows the cycling behaviors of $CaMoO_4$/Li test cell at different current rates. The $CaMoO_4$ nanocrystals display excellent cycling performance at a high rate, and a charge capacity of 276 and 438 mAh/g was delivered after 50 cycles in the range of 0.01–2.50 V vs metallic lithium at a current density of 100 and 200 mA/g, respectively. Average columbic efficiency at both current rates is no less than 98.0% from the second cycle to the 50th. Lithium ion diffusion became easier for full lithium intercalation and better current utilization due to smaller average grain size. Moreover, the cell is more stable at a current density of 200 mA/g than at 100 mA/g. It is different from the general electrode properties wherein lower current rate helps the stability. One cannot expect the aforementioned features in similar compounds prepared via conventional reaction [24, 26], which are very desirable for a material to be employed as electrode-active material in lithium ion batteries at high rate.

Conclusions

Rod-like $CaMoO_4$ nanocrystals were synthesized by a HMTA-assisted rheological phase reaction method. A structure-directed role of HMTA was observed during the crystal growth of $CaMoO_4$. Controlled synthesis of $CaMoO_4$ in nanoscale is a feasible means for optimizing electrode properties to achieve significant enhanced capacity and cycling performance at a high rate, which offers promises to enlarge the application of lithium ion batteries in high-power devices.

Acknowledgement This work was supported by the National Natural Science Foundation of China (20471044).

References

1. Conway BE (1999) Electrochemical supercapacitors. Kluwer/Plenum, New York
2. Rudge A, Davey J, Raistrick I, Gottesfeld S, Ferraris JP (1994) J Power Sources 47:89
3. Conway BE, Briss V, Wojtowicz J (1997) J Power Sources 66:1
4. Dahn JR, Zheng T, Liu Y, Xue JS (1995) Science 270:590
5. Wu YP, Wan C, Jiang C, Fang SB, Jiang YY (1999) Carbon 37:1901
6. Noel M, Santhanam R (1998) J Power Sources 72:53
7. Idota Y, Matsufuji A, Miyasaki Y (1997) Science 276:1395
8. Manthiram A, Tsang C (1996) J Electrochem Soc 143:L143
9. Dong QF, Wu CZ, Jin MG, Huang ZC, Zheng MS, You JK, Lin ZG (2004) Solid State Ionics 167:49
10. Wang CS, Appleby AJ, Little FE (2001) J Power Sources 93:17
11. Auborn JJ, Barberio YL (1987) J Electrochem Soc 134:638
12. Poizot P, Laruelle S, Grugeon S, Dupont L, Tarascon JM (2000) Nature 407:496
13. Denis S, Beudrin E, Touboul M, Tarascon JM (1997) J Electrochem Soc 144:4099
14. Martos M, Morales J, Sanchez L (2000) Electrochim Acta 46:83
15. Takeda Y, Kanno R, Tanaka T, Yamamoto O (1987) J Electrochem Soc 134:641
16. Hara D, Ikuta H, Uchimoto Y, Wakihara M (2002) J Mater Chem 12:2507
17. Jamnikab J, Maiera J (2003) Phys Chem Chem Phys 55:215
18. Poizot P, Laruelle S, Grugeon S, Dupont L, Tarascon JM (2000) Nature 407:496
19. Sun YK, Myung ST, Kim M, Prakash J, Amine K (2005) J Am Chem Soc 127:13411
20. Liang YG, Yang SJ, Yi ZH, Lei XF, Sun JT, Zhou YH (2005) Mater Sci Eng B 121:152
21. Roisnel T, Rodriguez-Carvajal J (2001) WinPLOTR: a Windows toll for powder diffraction patterns analysis Materials Science Forum, Proceedings of the European Powder Diffraction Conference (EPDIC7) 378:118
22. Boultif A, Louer D (2004) J Appl Cryst 37:724
23. Liang YG, Yi ZH, Yang SJ, Zhou LQ, Sun JT, Zhou YH (2006) Solid State Ionics 177:501
24. Kim SS, Ogura S, Ikuta H, Uchimoto Y, Wakihara M (2002) Solid State Ionics 146:249
25. Weast R (1986) CRC Handbook of Chemistry and Physics (67th ed), CRC, Boca Raton, Florida, pp D57–D75
26. Sharma N, Shaju KM, Subba Rao GV, Chowdari BVR, Dong ZL, White TJ (2004) Chem Mater 16:50